Supplementary Material for "The Ringed Structure of the HD 163296's disk revealed by ALMA"

Andrea Isella,[1] Greta Guidi,[2] Leonardo Testi,[2,3] Shangfei Liu,[1,4] Hui Li,[4] Shengtai Li,[4] Erik Weaver,[1] Yann Boheler,[1] John M. Carperter,[5] Itziar De Gregorio-Monsalvo,[5] Carlo F. Manara,[4] Antonella Natta,[6,7] Laura M. Pérez,[8] Luca Ricci,[9] Anneila Sargent,[10] Marco Tazzari,[3] and Neal Turner[11]

[1]*Department of Physics and Astronomy, Rice University, 6100 Main St., 77005, MS-108, Houston, Texas**

[2]*INAF-Osservatorio Astrofisico di Arcetri, Largo E. Fermi 5, 50125 Firenze, Italy*

[3]*ESO, Karl Schwarzschild str. 2, 85748 Garching bei Mnchen, Germany*

[4]*Theoretical Division, Los Alamos National Laboratory, Los Alamos, NM 87545, USA*

[5]*Joint ALMA Observatory (JAO), Alonso de Cordova 3107 Vitacura - Santiago de Chile, Chile*

[6]*School of Cosmic Physics, Dublin Institute for Advanced Studies, 31 Fitzwilliams Place, 2 Dublin, Ireland*

[7]*INAF/Osservatorio Astrofisico di Arcetri, Largo E. Fermi 5, I-50125 Firenze, Italy*

[8]*Max-Planck-Institut fr Radioastronomie Bonn, Auf dem Hgel 69, D-53121 Bonn, Germany*

[9]*Harvard-Smithsonian Center for Astrophysics, 60 Garden Street, Cambridge, MA 02138, USA*

[10]*Department of Astronomy, California Institute of Technology, MC 249-17, Pasadena, CA 91125, USA*

[11]*Jet Propulsion Laboratory, California Institute of Technology, Pasadena, CA 91109, USA*

(Dated: October 28, 2016)

DATA ACQUISITION AND CALIBRATION

HD 163296 was observed by ALMA on 2015 August 5, 8 and 9 at Band 6 using an array configuration that contained 37, 43, and 41 antennas respectively. The projected baselines spanned from 35 m to 1.57 km, resulting in a maximum recoverable size of $\sim 7''$ and an angular resolution of $\sim 0.2''$. J1733-1304 was used to calibrate for bandpass and phase, J1812-2836 was additionally observed every 20 minutes to calibrate the complex gains; Ceres and Titan were used as flux calibrators. The total integration time was $\sim$4.7 hours, with $\sim$2.5 hours on the science target.

The correlator was set up to four spectral windows in dual polarization mode, with SPW#1 centered at 231.587 GHz for the continuum (channel width of 15.6 MHz), and three SPWs at high spectral resolution (15.2 kHz, corresponding to $50\,\mathrm{m\,s^{-1}}$ after Henning smoothing): SPW #0 at 230.525 GHz including the CO J=2 - 1 transition, SPW #2 at 220.387 GHz including ^{13}CO J=2 - 1 transition, and SPW #3 at 219.548 GHz including the C^{18}O J=2 - 1 transition. Data were calibrated using the pipelines provided by ALMA, and self calibration was carried out with two rounds of phase calibrations and one of amplitude and phase on the continuum spectral windows of the three execution blocks, then applying the correction tables to both lines and continuum.

The continuum image was generated using the `CLEAN` algorithm in the `CASA` package (version 4.5.0) from the line free channels: we used a pixel size of $0.05''$ and a Briggs weighting parameter of -1 to obtain a synthesized beam of $0.22\times0.15''$ (PA = -88°). After subtracting the continuum in the visibilities space with the task `uvcontsub`, we produced spectral cubes for the three CO lines with a velocity resolution of $50\,\mathrm{m\,s^{-1}}$.

The angular resolution, rms noise, integrated flux, and peak flux of the dust continuum and spectrally averaged CO maps are listed in Table I.

PARAMETRIC MODEL OF THE DUST CONTINUUM EMISSION

We fit the normalized radial profile of the dust continuum emission with a combination of Gaussian functions, $f(\theta) = g(\theta) - g_1(\theta) - g_2(\theta) - g_3(\theta)$**, where** $g(\theta) = ae^{-(\theta/b)^2}$ **and** $g_n(r) = a_n e^{-((\theta-\theta_n)/b_n)^2}$**. The values of the best fit parameters are listed in Table II, while the comparison between the model and observations**

TABLE I. Summary of the continuum and emission line observations. Column 1: name of the observed species and transition. Column 2: reference frequency in GHz. Column 3: spatially integrated flux measured in the continuum (Jy) and in moment 0 of the line emission (Jy km s^{-1}). Column 4: peak flux measured in the continuum (Jy beam^{-1}) and in the moment 0 of line emission (Jy beam^{-1} km s^{-1}). Column 5 and 6: Full Width Half Maximum ($''$) and position angle ($^\circ$) of the synthesized beam. Column 7: robust parameter used for imaging the continuum and line emission. Column 8: root mean square noise measured in the continuum (Jy beam^{-1}) and in the moment 0 line emission (Jy beam^{-1} km s^{-1}).

Species	ν	F_{tot}	F_{peak}	FWHM, PA	rob	noise rms
continuum	231.58797	0.73150	0.0512	0.22×0.15, -89.8	-1	8.9e-5
^{12}CO J=2-1	230.53800	41.054	0.3414	0.22×0.16, -89.8	0	9.0e-3
^{13}CO J=2-1	220.39868	15.529	0.1152	0.23×0.17, -89.4	0	9.4e-3
C^{18}O J=2-1	219.56035	5.463	0.0756	0.24×0.17, -89.6	0	7.4e-3

is shown in Figure 1. The best fit parameters and related uncertainties are calculated performing a nonlinear least-squares Marquardt-Levenberg minimization accounting for the errors on the flux measurements.

DISK MODELS AND DATA ANALYSIS

In this section we describe the modeling procedure adopted to analyze ALMA observations. Our main goal is to investigate the nature of ringed structure observed in the continuum and the morphological differences between the continuum and the molecular line emission. We do this by comparing the radial profile of the continuum and CO emission with synthetic models for the disk emission. As a caveat, our analysis is performed by exploring the space of model parameters by hand. This choice is dictated by the fact that the large number of model parameters makes an exhaustive exploration of the parameter space extremely time consuming. As a consequence, the disk models presented below should not be considered to provide the best possible match to the observations. Nevertheless, we believe that this approach provides valuable clues to understand the main morphological features of the continuum and line emission. As a second caveat, we limit our analysis to the spectrally

TABLE II. **Best fit values and related 1σ uncertainties of the parametric model of radial profile of the dust continuum emission.**

Parameter	Value	Error
a	0.99	± 0.01
b	$0.76''$	$\pm 0.02''$
a_1	0.55	± 0.02
$\theta 1$	$0.44''$	$\pm 0.01''$
b_1	$0.23''$	$\pm 0.01''$
a_2	0.17	± 0.01
θ_2	$0.81''$	$\pm 0.01''$
b_2	$0.15''$	$\pm 0.01''$
a_3	0.06	$\pm$ 0.01
θ_3	$1.13''$	$\pm 0.02''$
b_3	$0.28''$	$\pm 0.02''$

integrated map of the molecular emission, and leave the analysis of the gas kinematics to a future paper.

Models for the dust emission

We start our analysis by searching for a model for the dust emission capable of reproducing the map of the continuum emission shown in Figure 1 of the main article. This choice is motivated by the fact that while the continuum image is recorded in a line-free region of the spectrum, the molecular line emission is always contaminated by the underlaying continuum. The interplay between line and continuum takes two main forms: first, molecules absorb continuum emission, such that the intensity of the continuum at frequencies covered by molecular lines is lower than the continuum at adjacent line-free wavelengths. This has a strong effect on the appearance of the continuum-subtracted line emission if both line and continuum are optically thick. **In this case ($\tau \gg 1$), the intensity of the continuum emission outside the line is proportional to the physical dust temperature T_d, while the intensity at the peak of the line is proportional to the physical gas**

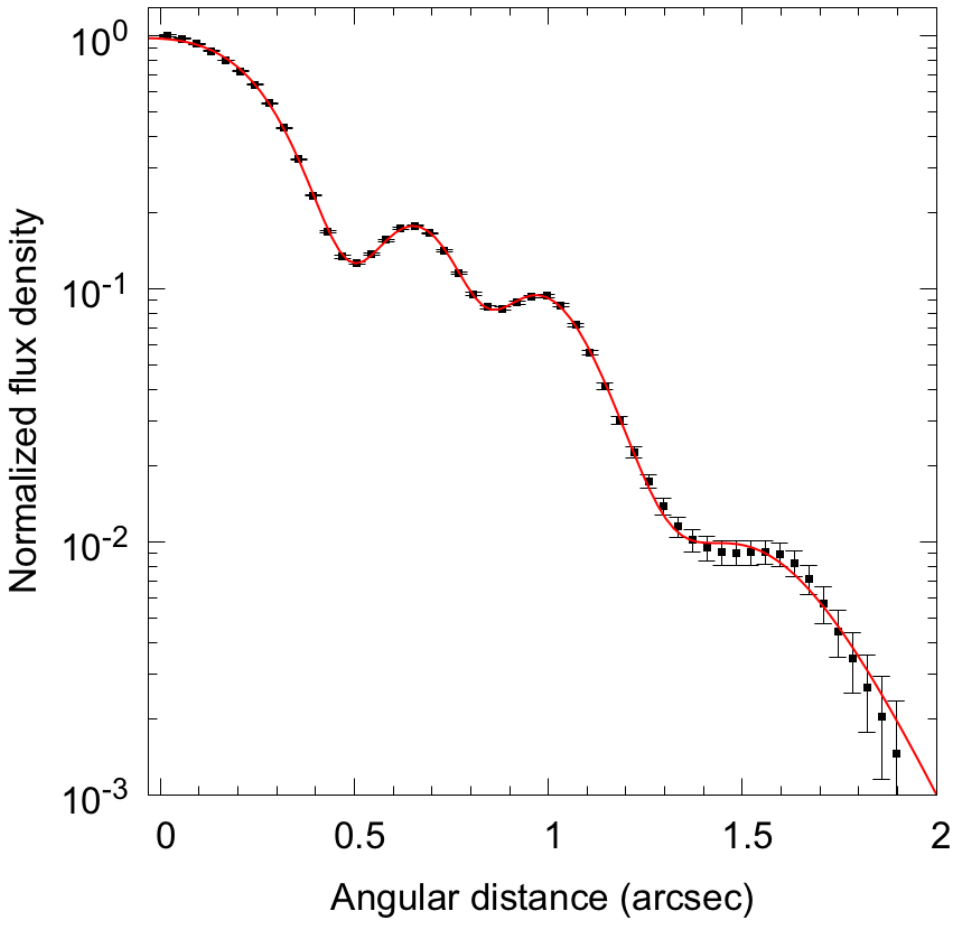

FIG. 1. Comparison between the azimuthally averaged profile of the dust continuum emission (symbols) and a parametric model based on a combination of Gaussian functions.

temperature T_g. This is different from the optically thin case ($\tau \ll 1$), in which the intensity of the continuum+line emission is proportional to $(T_g + T_d) \times \tau$**.** If $\tau \gg 1$, the line intensity in the continuum-subtracted image is therefore proportional to $T_g - T_d$, and not to T_g as in the optically thin case. Due to the positive vertical temperature gradient of an externally illuminated protoplanetary disk and to the higher opacity of CO molecules compared to dust grains, the layer corresponding to an optical depth of about 1 for the CO emission, i.e., the layer that emits most of the CO emission, is hotter that the layer emitting the dust continuum ($T_g > T_d$). As a result the CO line is observed in

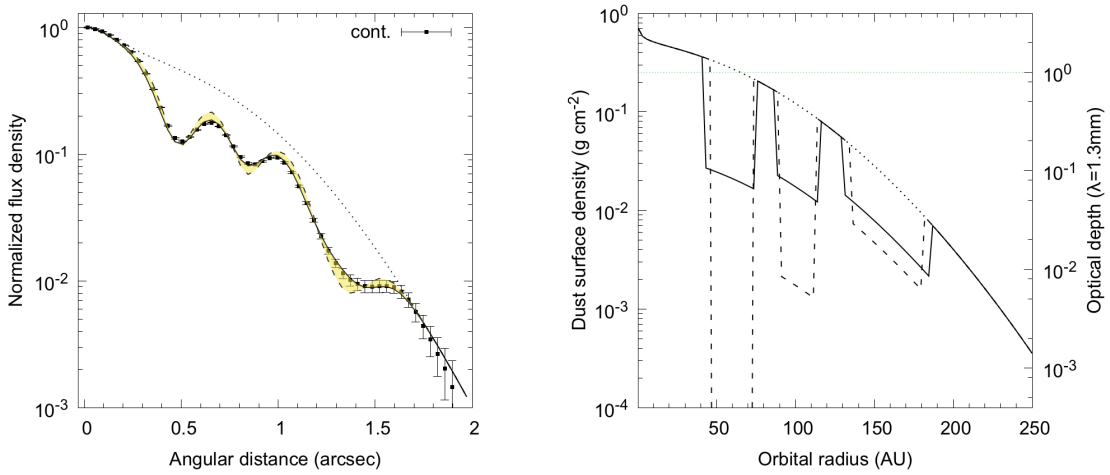

FIG. 2. Physical models for the dust continuum emission. The solid and dashed lines show the intensity (left) and surface density (right) of disk models characterized partially depleted gaps in the radial distribution of dust grains, while the dotted lines correspond to a disk model without gaps. The ringed structure observed in the continuum map is compatible with either narrow and deep gaps or wide and shallow gaps in the surface density profile. The two extreme cases are shown by the dashed and solid line respectively.

emission on top of the continuum. However, these two temperatures might be quite similar and therefore the continuum subtraction might actually remove a significant fraction of the line emission. For this reason, the interpretation of continuum-subtracted maps of optically thick lines requires caution. A second effect of the interplay between line and continuum emission is that the molecular emission can be absorbed by dust grains if the optical depth of the line is less than that of the dust. This happens if the abundance of the emitting molecule is very low and in the optically thin wings of optically thick lines, such as CO lines.

The interplay between continuum and line emission is complex when the disk emission is spatially resolved, as in the case of HD 163296, and the optical depths of line and continuum emission change with the distance from the star. For example, in the innermost disk regions where both continuum and line emission are optically thick, subtracting the continuum from the line+continuum emission results in underestimating the true line intensity. Moving away from the star, since the optical depth of the continuum drops faster than the optical depth of the line, the effect of the continuum subtraction becomes progressively less important.

Finally, in the disk outermost regions where both the line and continuum emission are optically thin, the continuum subtraction returns the true line intensity. As a result of this effect, integrated intensity maps of the continuum subtracted line emission are difficult to interpret. For example, in the case of HD 163296, the over subtraction of the continuum emission in the innermost disk regions leads to a decrement of the ^{13}CO and C^{18}O line emission toward the center of the disk, which might be confused for a chemical or physical effect. We will come back to this point in describing the comparison between models and observations.

We build our disk model upon the recent study of the HD 163296 disk performed by [1, R13 hereafter] and [2], which provide a good description of the ALMA science verification observations of the continuum and ^{12}CO (3-2) and (2-1), ^{13}CO (2-1), and C^{18}O (2-1) line emission observed at a resolution of about 0.6″. These observations have an angular resolution about three times coarser than our new observations and only marginally reveal the presence of substructures in the dust distribution [3].

In brief, the disk surface density and temperature are azimuthally symmetric and depend both on the cylindrical radius r and the distance z from the disk midplane through the Equations 1 and 2 in the main paper. The dust surface density is defined between an inner radius of 0.5 AU and an outer radius of 550 AU. The dust density along the direction perpendicular to the disk midplane is calculated by solving the equation of the hydrostatic equilibrium, and assuming that the sub-millimeter grains, i.e., the grains that dominate the opacity at the wavelength of the observations, are settled into a thin disk characterized by a scale height 10 times smaller than that of an hydrostatic equilibrium disk. In order to reproduce the ringed structure observed in the continuum, we carve three circular gaps in the dust density profile. For sake of simplicity, the gaps are rectangular in shape and are described by three parameters: the radius of the center of the gap (R), the full width of the gap (W), and the depth of the gap expressed in units of the non-depleted surface density at the center of the gap (Δ). For each choice of dust surface density, we use the ray tracing module of RADMC-3D [4] to calculate synthetic images of dust continuum emission assuming a dust opacity at 1.3 mm of 3.95 cm^2 g^{-1}, which corresponds to a typical dust opacity for astronomical grains with a grain size distribution extending up to 1 mm [5].

Figure 2 shows two models that reproduce the continuum map. In both of them, the dust surface density is characterized by $\gamma = 0.1$, $r_c = 90$ au, and $\Sigma_c = 0.42$ g cm^{-2}. The

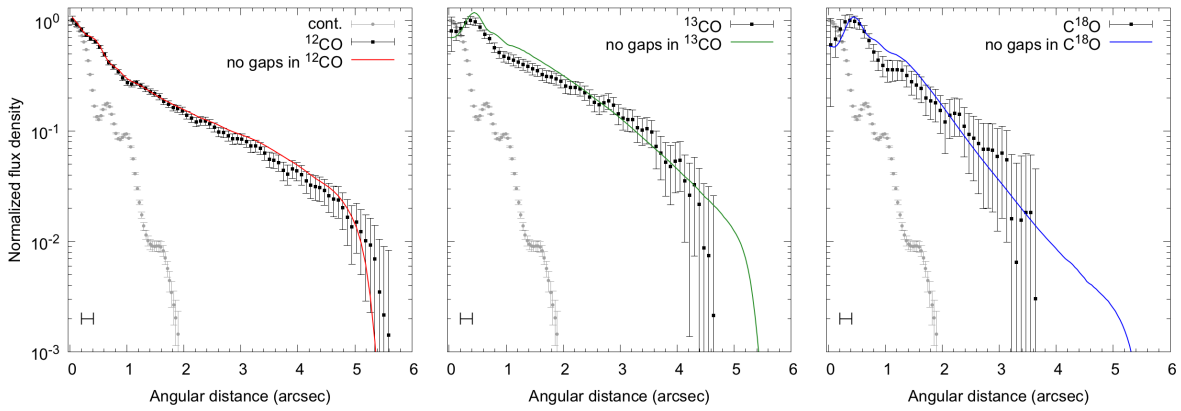

FIG. 3. Comparison between the observations and models for the ^{12}CO (left), ^{13}CO (center), and C^{18}O (right) J=2-1 line emission which do not include any radial gap in the gas density. The solid lines show the radial profile of the CO emission for a disk model characterized by a monotonically decreasing density of CO molecules and a dust surface density with partially depleted gaps as described by the solid curve of the right panel of Figure 2. The radial profile of the dust continuum emission is shown with gray symbols as a reference. The angular resolution of the observations is shown by the horizontal bar on the bottom left of each panel.

total dust mass integrated between 0.5-550 AU is 6.5×10^{-3} M$_\odot$. This surface density profile has the same γ and mass of that derived by [2] using lower angular resolution data, but a smaller characteristic radius (90 au instead of 125 au). The uncertainties on γ^d, r_c^d, and the total dust mass appear to be around $\pm$10%. However a statistical exploration of the model parameters, e.g., through a MCMC analysis as in [6], is necessary to properly investigate the degeneracies between all the model parameters.

The centers of the three dust depleted gaps are at $R_1 = 60$, $R_2 = 100$, and $R_3 = 160$ AU. Given the finite angular resolution of the observations, there is a degeneracy between the width and the depth the dust gaps, such that we cannot distinguish between deep and narrow or wide and shallow gaps. Two extreme cases are shown by the dashed and solid curves, respectively. The narrowest gaps compatible with the observations have full widths of $W_1 = 25$ AU, $W_2 = 22$ AU, and $W_3 = 45$ AU, and depletion factors of $\Delta_1 > 100$, $\Delta_2 = 70$, and $\Delta_3 = 6$, respectively. The widest gaps have widths of $W_1 = 33$ AU, $W_2 = 26$ AU, and $W_3 = 55$ AU, and depletion factors $\Delta_1 = 13$, $\Delta_2 = 7$, and $\Delta_3 = 3.6$.

Models for the CO emission

Having found a suitable family of models for the dust emission, we now proceed to search for gas emission models able to reproduce the main morphological features of the observed CO emission. In our model, we set the surface densities of ^{12}CO, ^{13}CO, and C^{18}O independently using Equation 1 of the main paper. However, the three CO isotopologues share the same temperature described using Equation 2 of the main paper. The CO density along the vertical direction is then calculated from the surface density and temperature by solving for the equation of the hydrostatic equilibrium. As in R13, we mimic the CO freeze-out by setting the molecular abundance to zero where the gas temperature is less than 19 K. Furthermore, the CO density is reduced by a factor of 10^8 in the disk surface to account for photodissiociation. To calculate the frequency dependent CO emission, we assume that the gas is rotating at Keplerian velocity and that the central star has a mass of 2.3 $M_\odot$.

The CO emission is calculated by using the ray tracing module of RADMC-3D, under the assumption that the CO molecules are in Local Thermodynamic Equilibrium. For each line, we generated synthetic images of the total (line+continuum) and continuum-only emission at 71 velocities between -6 to +6 km/sec. The disk models are inclined by 42° and rotated by 132° to match the orientation of the HD 163296 disk. The same inclination and position angle was used to produce the models for the dust continuum emission discussed above. Continuum-subtracted maps of the CO emission are then obtained by subtracting the line-free dust continuum emission from the total emission. This latter step is critical to avoid underestimating the line emission in the optically thick disk regions as discussed above. The continuum-subtracted cubes are smoothed at the resolution of the observations, spectrally integrated, and azimuthally averaged following the same procedure adopted to analyze the observations. **Since the radial extent of the CO emission measured from the channel maps presented in R13 is smaller than the maximum recoverable scale of our observations, we neglect the effect of the spatial filtering.** We tweak by hand the model parameters that control the gas temperature and density until we find a satisfactory fit to the observations. Although this heuristic approach to model fitting has important drawback, it is here justified by the fact that the calculation of a single full model, which includes maps of dust continuum emission as well as spectral cubes of the ^{12}CO, ^{13}CO, and C^{18}O J=2-1 emission, requires several cpu hours.

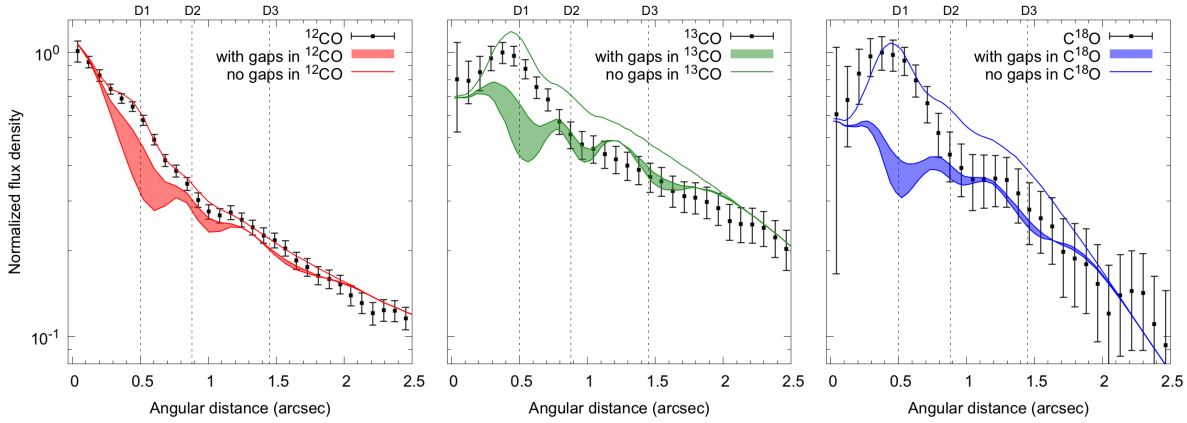

FIG. 4. Comparison between the observations and models for the ^{12}CO (left), ^{13}CO (center), and C^{18}O (right) J=2-1 emission including CO depleted gaps equal to those inferred from the dust emission. The width of the colored lines indicates the intensity range corresponding to the gap models consistent with the continuum emission. The solid lines are as in Figure 4 and show the predicted emission for a disk model without gaps in the CO surface density and gaps in the dust surface density.

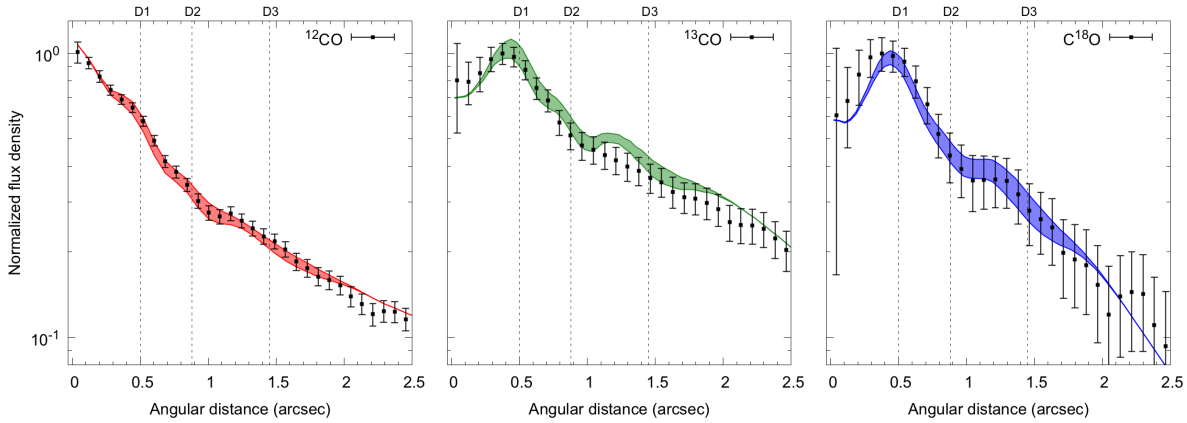

FIG. 5. The solid points are as in Figure 5. The colored regions show the radial profile of the CO emission for disk models in which the CO depletion factor has been tuned to match the observations as discussed in the text.

We start our analysis by noting that the lack of prominent rings in the CO intensity maps either suggests the absence of depleted gaps in the distribution of CO molecules, or,

perhaps, that such gaps exist but their observability is hampered by the large optical depth of the line emission. To investigate the first point, we compare the radial profile of the CO emission to a disk model characterized by a monotonically decreasing gas surface density profile without gaps. As for the dust surface density, we adopt the model with narrow gaps described above. We find a good match to the observations using $\gamma = 0.8$ and $r_c = 165$ au for all three CO isotopologues, and $\Sigma_c(^{12}\mathrm{CO}) = 1.6 \times 10^{-3}$ g cm^2, $\Sigma_c(^{13}\mathrm{CO}) = 2.3 \times 10^{-5}$ g cm^2, and $\Sigma_c(\mathrm{C}^{18}\mathrm{O}) = 2.9 \times 10^{-6}$ g cm^2. The density ratio between CO isotopologues are $^{12}\mathrm{CO}/^{13}\mathrm{CO} = 70$ and $^{12}\mathrm{CO}/\mathrm{C}^{18}\mathrm{O} = 552$. **Our results are in good agreement with [7], who found $^{12}\mathrm{CO}/^{13}\mathrm{CO} = 68 \pm 8$ and $^{12}\mathrm{CO}/\mathrm{C}^{18}\mathrm{O} = 557 \pm 30$.** The total mass of ^{12}CO is 2.5×10^{-5} M$_\odot$.

The synthetic intensity profile of this model is shown in Figure 3. It reproduces remarkably well both the total flux and the radial profile of the ^{12}CO emission but it over predicts the ^{13}CO and C^{18}O emission arising from disk regions between about 0.6″–2″ from the star, which correspond to the location of the middle and outer continuum dark rings. Even if the density and temperature of ^{13}CO and C^{18}O molecules increases toward the center of the disk, our model reproduces the central decrement of the observed emission. As discussed above, this decrement is caused by the over-subtraction of the continuum emission in disk regions where both the CO line and the dust continuum is optically thick. We ran about 200 models for the dust and CO emission changing both the gas density and temperature. We found that the surface densities of ^{12}CO and ^{13}CO are uncertain by about 10-20%, while the uncertainty on the C^{18}O surface density can be as large as 30%.

Our model suggests that most of the ^{12}CO and ^{13}CO emission is optically thick throughout the disk and therefore provides a powerful tool to estimate of the gas temperature. A good fit of the observations is obtained adopting a disk midplane temperature $T_m(r) = 24\mathrm{K}(r/100\mathrm{au})^{-0.5}$ and a disk surface temperature $T_a(r,z) = 68\mathrm{K}(\sqrt{r^2+z^2}/100\mathrm{au})^{-0.6}$. The transition between these two layers is set by the function $\delta(r) = 0.0034 \times (r - 200\mathrm{au}) + 2.5$, and $z_q(r) = 63\mathrm{au}(r/200\mathrm{au})^{1/3} \exp -(r/800\mathrm{au})^2$. The midplane temperature of our model is about 10% warmer compared to the model discussed in R13, while the surface temperature is about 10% colder. The fact that the temperature model of R13 provides a significantly worse fit to the observations suggest that the CO emission constrains the gas temperature within about 10%.

As a next step, we introduce gaps in the CO surface density and recalculate the spectrally

averaged radial profile of the ^{12}CO, ^{13}CO, and C^{18}O J=2-1 line emission. In this set of models, dust and CO are depleted by the same amount inside the gaps, but we do not change the gas temperature. The results are shown in Figure 4. We find that the reduction of CO molecules produces a drop in the corresponding emission between about 0.2″ and 2″ from the central star. The emission decrement is the largest for the C^{18}O line due to its lower optical depth compared to the other two lines. These models provide a better match to the ^{13}CO and C^{18}O emission across the middle and outermost gaps, but predict too little line emission at the position of the innermost dust gap. We then compare the observations with models in which the CO density inside the dust gaps is less depleted than the dust itself. We explored a wide range of CO depletion factors for the two extreme dust gaps configurations shown in Figure 2. In the case in which the gaps are the widest, we find a good match between models and observations for CO depletion factors between 0-2.5 in D1, 3.5-7 in D2, and 1.8-3.6 in D3 (Figure 5). These values should be compared to the dust depletion factors of 13 in the inner gap, 7 in the middle gap, and 3.6 in outer gap. In the case in which the gaps are the narrowest, we obtain CO depletion factors between 0-2.5 in the inner gap, 30-70 in middle gap, and 3-6 in the outer gap, compared to dust depletion factors > 100, 70, and 6, respectively.

Finally, Figure 6 shows a comparison between the observed maps of the dust and CO emission and those relative to one of the synthetic disk models that reproduces the observed intensity profiles. Overall, we find that the residuals are small compared to the observed emission. This supports the choice of adopting azimuthally symmetric models for the analysis of the observations. However, some properties of the residual maps are worth a mention. Concerning the continuum, the residuals have amplitudes less than $\pm$10% of the observed flux, **but nevertheless higher than 5$\times$ the noise level**. The residuals are the highest in the north-west part of the disk suggesting that the dusty ring might be eccentric. **The residuals of the ^{12}CO emission are also significant compared to the noise,** and show that the south west-side of the disk is about 10% fainter than the north-east side. Finally, the ^{13}CO and C^{18}O residuals are negative on the north-east side of the disk very close to the center, suggesting that an azimuthally symmetric model does not properly reproduce the structure or kinematics of the innermost molecular disk. A detailed investigation of the asymmetries in the HD 163296 disk is beyond the scope of this letter and is left for a future work.

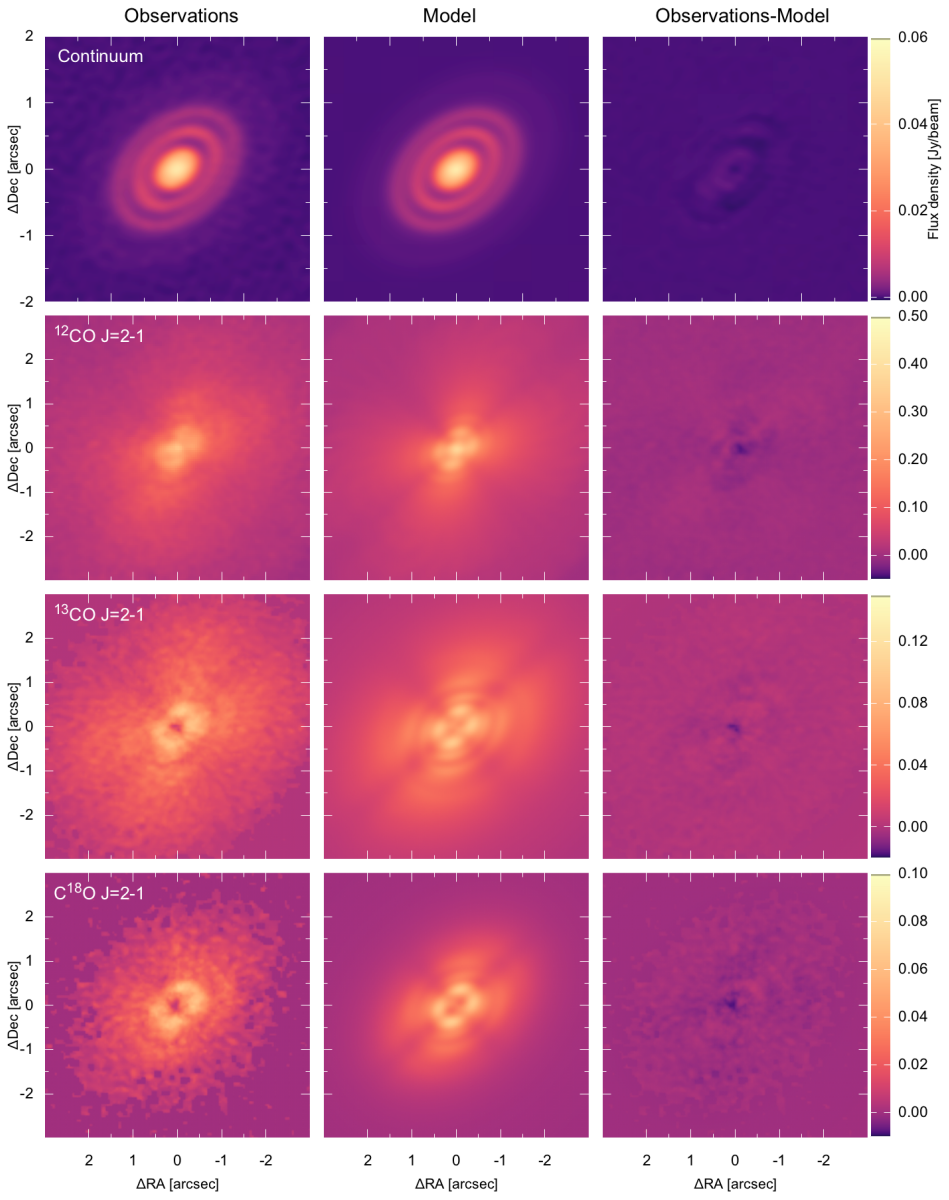

FIG. 6. Comparison between observations and models. The panels in the left column show the continuum image as well as the maps of the integrated line emission. The panels of the central column show maps of the synthetic model emission convolved with the synthesized beam of the observations. Finally, the panels of the right column show the maps of the residual obtained by subtracting models from observations.

HYDRODYNAMIC SIMULATIONS OF THE PLANET-DISK INTERACTION

The effect of the planet gravity on the gas and dust surface density in the HD 163296 disk was calculated by solving the two-fluid equation for the gas+dust+planet disk system surrounding a star, using the LA-COMPASS code [8–11]. We initialize the hydrodynamic simulation using the gas surface derived from the ^{12}CO emission ($\gamma = 0.8$, $r_c = 165$ au, $\Sigma_c(^{12}\mathrm{CO}) = 1.6\times10^{-3}$ g cm^{-2}) multiplied by a radially constant ratio $H_2/^{12}\mathrm{CO} = 1400$. The temporal evolution of the disk density and kinematics is calculated assuming an isothermal equation of state and the disk temperature discussed in the previous section. We inject fully formed planets in the disk and we keep them at fixed orbital radii for the entire length of the simulation. Initially, the radial profiles of the gas and dust surface density are equal, and we assume a gas-to-dust ratio of 100. Since the ALMA observations of HD 163296 probe the distribution of sub-millimeter grains, we assume a nominal grain size of 0.15 mm, which corresponds to a Stokes number of about 0.015 at 100 AU from the star. The presence of such large grains in the HD 163296 disk has been inferred from multi-wavelength observations [3]. For our 2D $\{r, \phi\}$ simulations, we use 3072×1024 grid on $[0.24, 7.92] \times [0, 2\pi]$ in the radial and azimuthal directions, respectively. **Radially, the cells are linearly spaced and have a physical size of 0.15 au.** Dust is treated as pressureless fluid. Its back-reaction on gas is included. A dust diffusion model in the dust continuity equation to model the turbulent motion is included as well. We typically run our simulations to 2000 orbits at 62 au. This disk is still evolving (especially at large radii) though the lifetime of 7×10^5 yr is a reasonable estimate for the joint planet-disk evolution.

We have carried $\sim$ 100 2D hydrodynamic simulations using various planet masses and disk profiles, including the effects of disk viscosity. We typically find that the joint dust and gas emissions are providing much stronger constraints on the two-fluid evolution of gas+dust in disks. The disk is assumed to have a Shakura-Sunyaev viscosity parameter α that increases with the radius as

$$\alpha(r) = \alpha_2 \left(1 - \frac{(1-\alpha_1/\alpha_2)(1-\tanh\frac{r-150}{R_0})}{2} \right), \quad (1)$$

where $\alpha_1 = 5\times10^{-5}$, $\alpha_2 = 1.5\times10^{-2}$, and $R_0 = 60$ AU. The values of these parameters are chosen so that they give reasonable fits to both observed dust and gas distributions. This generic trend of $\alpha(r)$ is consistent with the results in [12], though the transition radius of

150 au adopted in our simulations is larger than the estimated value of 100 au. The values of parameters in our simulations are chosen so that they give reasonable fits to both observed dust and gas distributions.

We find that the gas and dust surface density measured across the middle and outer gaps are compatible with the perturbation exerted by two 0.3 M_J planets orbiting at 105 au and 160 au from the central star, respectively, and $10^{-3} < \alpha < 10^{-2}$. A lower value of α in the innermost part of the disk is required to give better fits to the width, the gas depletion, and gas-to-dust ratio measured within the inner dust gap. However, even in this case, we find that the a single planet interaction model does not properly explain the observed characteristics of the inner gap.

* isella@rice.edu

[1] K. A. Rosenfeld, S. M. Andrews, A. M. Hughes, D. J. Wilner, and C. Qi, Astrophys. J. **774**, 16 (2013), arXiv:1306.6475 [astro-ph.SR].

[2] I. de Gregorio-Monsalvo, F. Ménard, W. Dent, C. Pinte, C. López, P. Klaassen, A. Hales, P. Cortés, M. G. Rawlings, K. Tachihara, L. Testi, S. Takahashi, E. Chapillon, G. Mathews, A. Juhasz, E. Akiyama, A. E. Higuchi, M. Saito, L.-Å. Nyman, N. Phillips, J. Rodón, S. Corder, and T. Van Kempen, Astron. Astrophys. **557**, A133 (2013), arXiv:1307.1357 [astro-ph.SR].

[3] G. Guidi, M. Tazzari, L. Testi, I. de Gregorio-Monsalvo, C. J. Chandler, L. Pérez, A. Isella, A. Natta, S. Ortolani, T. Henning, S. Corder, H. Linz, S. Andrews, D. Wilner, L. Ricci, J. Carpenter, A. Sargent, L. Mundy, S. Storm, N. Calvet, C. Dullemond, J. Greaves, J. Lazio, A. Deller, and W. Kwon, Astron. Astrophys. **588**, A112 (2016), arXiv:1601.07542 [astro-ph.SR].

[4] C. P. Dullemond, "RADMC-3D: A multi-purpose radiative transfer tool," Astrophysics Source Code Library (2012), ascl:1202.015.

[5] A. Isella, L. Testi, A. Natta, R. Neri, D. Wilner, and C. Qi, Astron. Astrophys. **469**, 213 (2007), arXiv:0704.0616.

[6] A. Isella, J. M. Carpenter, and A. I. Sargent, Astrophys. J. **701**, 260 (2009), arXiv:0906.2227 [astro-ph.SR].

[7] C. Qi, P. D'Alessio, K. I. Öberg, D. J. Wilner, A. M. Hughes, S. M. Andrews, and S. Ayala, Astrophys. J. **740**, 84 (2011), arXiv:1107.5061 [astro-ph.SR].

[8] H. Li, S. Li, J. Koller, B. B. Wendroff, R. Liska, C. M. Orban, E. P. T. Liang, and D. N. C. Lin, Astrophys. J. **624**, 1003 (2005), arXiv:astro-ph/0503404.

[9] S. Li and H. Li, Technical Report, LA-UR-09-2968 (2009).

[10] W. Fu, H. Li, S. Lubow, and S. Li, Astrophys. J. Lett. **788**, L41 (2014), arXiv:1405.7379 [astro-ph.EP].

[11] W. Fu, H. Li, S. Lubow, S. Li, and E. Liang, Astrophys. J. Lett. **795**, L39 (2014), arXiv:1410.4196 [astro-ph.EP].

[12] X.-N. Bai, Astrophys. J. **821**, 80 (2016), arXiv:1603.00484 [astro-ph.EP].